Impeller optimization using a machine learning-based algorithm with dynamic sampling method and flow analysis for an axial flow pump

Impeller optimization using a machine learning-based algorithm with dynamic sampling method and flow analysis for an axial flow pump

Xueyi Song[1], Ying Li[2], Renfang Huang[3] and Xianwu Luo[1*]

[1] State Key Laboratory of Hydroscience and Engineering, Department of Energy and Power Engineering, Tsinghua University, Beijing 100084, China. songxy19@mails.tsinghua.edu.cn

[2] Chinergy Co.,Ltd., Beijing, 100193, China. Yingli01@chinergy.com.cn

[3] Key Laboratory for Mechanics in Fluid Solid Coupling Systems, Institute of Mechanics, Chinese Academy of Sciences, Beijing, 100190, China

*luoxw@tsinghua.edu.cn

Abstract. Design optimization for widely used axial flow pumps presents a formidable challenge due to the significant impact of numerous parameters associated with impeller geometry on hydraulic performance. The expansive design space raises concerns about the cost and time implications of the optimization process. This paper introduces a machine learning-based algorithm with a dynamic sampling approach to enhance the hydraulic performance of axial flow pumps. The focus is on an axial flow pump designed for China's South-to-North Water Diversion Project. Optimization involves selecting 15 design variables governing impeller geometry, considering meridional shape and mean blade profiles. The optimization process predicts hydraulic performance using CFD methods, with a primary objective of maximizing efficiency at the axial flow pump's design point while maintaining pump head around the design value. The results indicate that the proposed machine learning-based algorithm exhibits commendable convergence, delivering a notable improvement in performance. For instance, the optimized axial flow pump displays 2% efficiency increase compared to the initial design. Further analysis employing concepts like entropy generation rate and boundary vorticity flux reveals that the optimized pump has more uniform flow near the pressure side of the impeller blade. Additionally, design optimization effectively suppresses flow separation at the blade trailing edge near the impeller hub. This study offers valuable insights and a practical tool for the design optimization of axial flow pumps.

1. Introduction

The axial flow pump has wide and important applications in various industries such as marine propulsion, water diversion [1-4], etc. for its large flow discharge. In the past, the design optimization of the axial flow pump relied on engineers' expertise [5-8]. The traditional optimization procedure involves an iterative loop where geometry parameters are revised manually to achieve the desired pump performance through numerical calculations or experimental tests till meeting the requirements

[9]. Due to a multitude of geometry parameters of the axial flow pump, it is not easy to consider all of them simultaneously [10-12]. Consequently, optimizing such pumps, with their expansive design space, solely through trial and error becomes an exceedingly challenging task. Though orthogonal testing aims to comprehensively incorporate critical factors and minimize trial iterations, its coupling with the optimization process consumes huge computational resources [13-15].

With the rapid advancement of computational technology, various numerical techniques have been applied for turbo machinery optimization. For instance, the genetic algorithm [16-23] has found widespread application in the optimization of pumps. Huang et al. introduced a modified version of the non-dominated sorting genetic algorithm II (NSGA-II) coupled with a dynamic crowding distance (DCD) method for multi-objective optimization of a mixed-flow pump impeller. The results showed an optimized impeller with improved hydraulic efficiency of 92% and higher impeller head at the design operation point [24]. Ghadimi et al. employed a metamodel-assisted genetic algorithm to enhance efficiency and minimize blood damage in a centrifugal blood pump. They focused on optimizing key dimensions of the base design, including inlet and outlet radii, blade angle distributions, and volute cross-section area [25]. Shojaeefard et al. utilized NSGA-II to optimize a centrifugal pump inducer, leading to a 14.3% increase in head coefficient and a 0.3% increment in hydraulic efficiency for the inducer [26]. While the genetic algorithm excels in efficiently locating global optima, its shortcomings include sluggish convergence and substantial resource consumption. The genetic algorithm often demands numerous design iterations to navigate towards the global optimum region, which can be time-consuming, particularly when coupled with CFD simulations for performance assessment.

In recent times, machine learning-based surrogate models are used as alternatives to CFD simulations [27-34] to address this challenge. For instance, Wang et al. [35] utilized an artificial neural network to optimize a double suction centrifugal pump. This network was built using Design of Experiments (DoE), providing a readily computable surrogate space. However, the optimization process revealed that a substantial number of sampling points are required to establish an accurately predictive surrogate model, which could result in excessive points in less promising regions. To advance machine learning-driven design optimization, there's a need for sophisticated algorithms capable of not only approaching the global optimum point more closely but also converging to it more rapidly. For examples, Owoyele et al. [36] introduced a machine learning-driven optimization technique for internal combustion engine design. Unlike other machine learning-based approaches, Owoyele's method significantly diminishes the need for computationally intensive sampling far from the global optimum. This is achieved by eliminating reliance on an initial Design of Experiments (DoE) to train the machine learning surrogate models. Notably, in the realm of internal combustion engine design, this approach has demonstrated remarkable sample efficiency in locating the global optimum [37]. Similarly, Song et al. [38] employed a machine learning-based optimization algorithm with a dynamic sampling approach to optimize airfoil designs, and this was compared with the traditional genetic algorithm. The results indicate that the machine learning-based method yields superior aerodynamic performance and optimization efficiency compared with the conventional genetic algorithm approach.

The primary objective of this study is to introduce a machine learning-based optimization algorithm with a dynamic sampling approach suitable to improve hydraulic performance of an axial flow pump designed for the South-to-North Water Diversion Project in China. The specific speed of the axial flow pump is 850 r/min·m^3/s·m. The optimization process focuses on various factors, including the meridional section of pump impeller, blade profiles at different spans, etc. Hydraulic performance as well as internal flow for the baseline model and the optimized models is predicted by numerical simulation. Through comparison, performance improvement and flow features of the optimized axial flow pump are further discussed.

2. Optimization problem

2.1. The baseline pump configuration

The study aims to optimize an axial flow pump impeller for the South-to-North Water Diversion project in China. Note that diffuser vanes are not included in the flow passage of the axial flow pump for convenience. The detailed operating condition and the main geometrical parameters of the axial flow pump are listed in Table 1. The baseline model of the axial flow pump designed based on the conventional method [39] has flow rate of Q_d=374l/s and head of H_d=8m at the designed point when operated at the rotational speed of n=1450r/min. In the following text, the baseline model of the axial flow pump is called as the initial pump.

Table 1. Parameters for the axial flow pump.

Parameters	Symbol	Value
Pump casing diameter (mm)	D	300
Diameter at impeller hub (mm)	d_h	125
Diameter at impeller shroud (mm)	D_t	299.4
Clearance at impeller blade tip (mm)	c	0.3
Number of impeller blade	Z	4
Flow rate at designed operation (l/s)	Q_d	374
Pump head at designed operation (m)	H_d	8
Rotational speed of pump impeller (r/min)	n	1450
Fluid temperature (°C)	T	20

2.2. Optimization objectives

For the purpose of saving energy, the pump efficiency is set as the main optimization objective in this study. In order to satisfy the operation condition of axial flow pump, the pump head should be not less than the designed value at Q_d. Further, it is necessary to restrict the pump head not larger than the value of $1.2H_d$.

2.3. Design variables

When optimizing the impeller, it becomes essential to establish a mathematical representation for the blade profile. This allows the geometrical parameters of the blade profile to function as design variables, effectively translating the physical space into a design space. In this study, both the meridional section and the mean camber line at each span of impeller blade are integrated into the optimization procedure.

The schematic illustration of the meridional section for the axial flow pump impeller is presented in Figure 1. Concerning the meridional section, the diameters at the hub i.e. d_h and at the shroud i.e. D of the axial pump impeller are maintained as constants. During the optimization of the impeller's meridional section, adaptability is introduced to modify both the leading and trailing edges. As examples, design variables encompass axial positions of the leading edge at the hub i.e. $Z_{le,h}$ and that at the shroud i.e. $Z_{le,s}$, along with axial positions of the trailing edge at the hub i.e. $Z_{te,h}$ and that at the shroud i.e. $Z_{te,s}$ are selected as design variables. Furthermore, the leading and trailing edge curves are defined utilizing second-order Bezier curves.

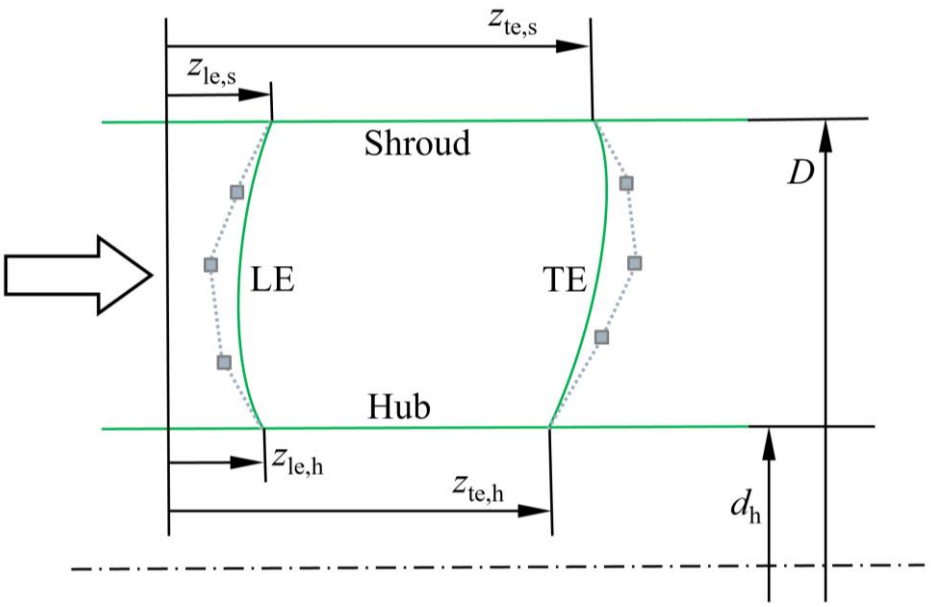

Figure 1. Schematic of the meridional section for axial impeller.

The mean camber lines at various spans for the axial flow pump impeller blade is presented in Figure 2, where the horizontal axis represents the blade wrap angle, while the vertical axis denotes the streamline's length on the meridional section. It's worth noting that the blade wrap angle indicates the circumferential position of the blade. As observed, 5 spans are utilized for the design of impeller blade. For each span's mean camber line, a second-order Bezier curve is utilized to shape these lines. Design variables encompass the intersections of the mean camber line's leading and trailing edges with the hub and shroud in the meridional direction. Typically, the blade angle at the leading edge significantly influences pump performance, with the inclusion of the incidence angle i.e. Δi being crucial for design optimization. The incidence angle Δi is the difference between the setting angle and the flow angle at blade leading edge. Additionally, the blade angle at the trailing edge introduces the concept of the slip angle i.e. $\Delta\delta$ as a significant consideration for impeller design optimization. Importantly, the slip angle $\Delta\delta$ denotes the disparity between the blade angle at impeller exit and the flow angle computed using Euler's equation for pumps. Both the incidence angles and the slip angles at the hub and shroud are designated as design variables in this study.

In order to obtain the physically valid impeller geometry and guarantee a smooth surface of pump impeller, the parameters for other spans are computed by using the linear interpolation, after the data at the hub and shroud have been determined. The interpolation of impeller geometry is helpful to reduce the design variables.

The design variables used for optimization of the blade in this study are listed in Table 2. It can be seen that 15 design variables are used for blade optimization of the pump impeller.

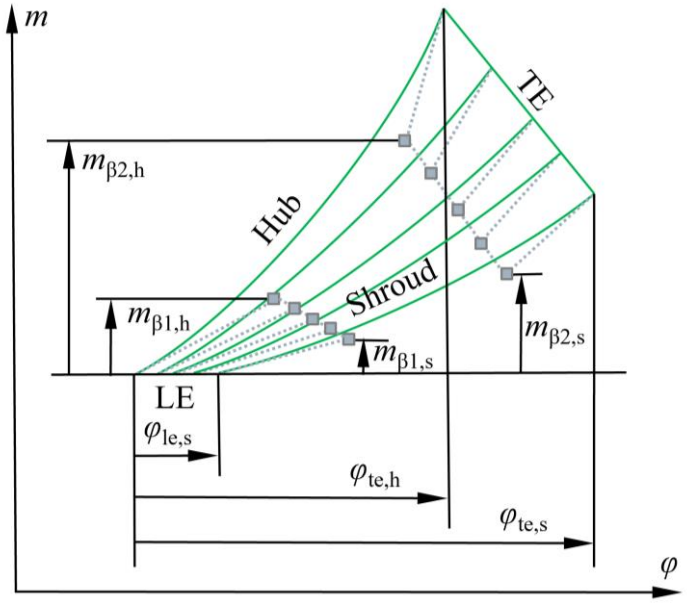

Figure 2. Mean camber lines at different spans for axial blades.

Table 2. Design variables and its limits for axial impeller blade optimization.

Parameters	Symbol	Lower limit	Upper limit
Position of start control point for mean camber line at hub in meridional direction	$m_{\beta 1,h}$	5%	40%
Position of end control point for mean camber line at hub in meridional direction	$m_{\beta 2,h}$	50%	95%
Position of start control point for mean camber line at shroud in meridional direction	$m_{\beta 1,s}$	5%	40%
Position of end control point for mean camber line at shroud in meridional direction	$m_{\beta 2,s}$	50%	95%
Circumferential angle at leading edge of mean camber line at shroud	$\varphi_{le,s}$	0°	30°
Circumferential angle at trailing edge of mean camber line at hub	$\varphi_{te,h}$	50°	100°
Circumferential angle at trailing edge of mean camber line at shroud	$\varphi_{te,s}$	50°	100°
Position of leading edge at shroud	$z_{le,s}$	0.1mm	48mm
Position of trailing edge at shroud	$z_{te,s}$	50mm	118mm
Position of leading edge at hub	$z_{le,h}$	5mm	24mm
Position of trailing edge at hub	$z_{te,h}$	40mm	110mm
Incidence angle at hub	Δi_{hub}	-25°	25°
Incidence angle at shroud	Δi_{shroud}	-25°	25°
Slip angle at hub	$\Delta\delta_{hub}$	0	35°
Slip angle at shroud	$\Delta\delta_{shroud}$	0	35°

2.4. Design space

When optimizing axial flow pump impellers, the extent of the design space often has an influence on the speed of convergence during the optimization process, particularly when employing stochastic search techniques like NSGA-II [24]. However, in this study, the machine learning-based algorithm utilized for axial flow pump impeller optimization is deterministic. As such, the influence of the design space on the convergence speed of the optimization process remains relatively limited. This implies that the computational cost does not escalate sharply with an expanded design space. Consequently, to achieve improved optimization results, the design space is configured to ensure that the optimal value falls within the region under consideration. The lower and upper limits for the design variables are detailed in Table 2.

3. Numerical methods

3.1. Computational domain

To assess the hydraulic performance of the axial flow pump during optimization process, numerical simulations have been conducted. The computational domain of the flow passage includes the inlet pipe, impeller, and outlet pipe, as shown in Figure 3. Note that the pump is of axial type, with a specific speed of 850 r/min·m^3/s·m according to the definition $n_s = 3.65n\sqrt{Q}/H^{3/4}$. Because there is a gap between the tip of impeller blade and the pump casing, the impact of tip clearance on the hydraulic performance of the pump is taken into consideration in numerical simulation.

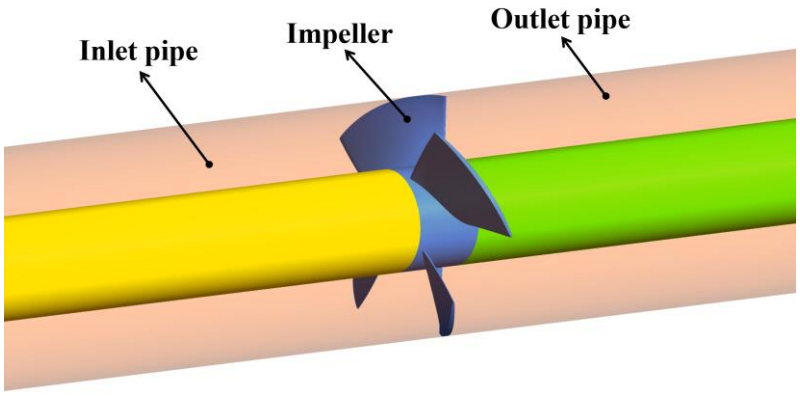

Figure 3. Computational domain for an axial flow pump.

3.2. Mesh generation and independence test

The entire domain's mesh is generated using the structural hexahedral mesh by using the commercial software ANSYS-ICEM, ensuring that the value of y^+ falls within the range of 50. The structural hexahedral mesh created for the impeller is illustrated in Figure 4. This visualization reveals the grid refinement near the solid walls, with particular attention to the region surrounding the impeller blade.

A mesh independence test is conducted, involving adjustments to mesh densities to simulate steady flow at the designed flow rate. As indicated in Table 3, both the pump head and efficiency exhibit gradual increases with an escalating number of grid points, stabilizing when reaching a grid count of 5.98 million. Consequently, the total grid of 5.98 million is selected for the simulation of the internal flow within the pump.

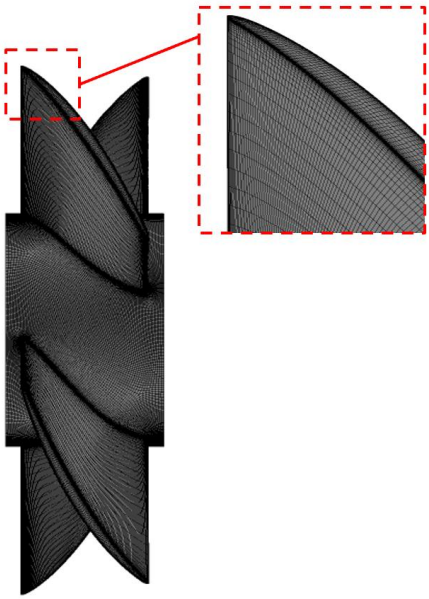

Figure 4. Grid distribution for axial flow pump impeller.

Table 3. Mesh independence test for the pump.

Mesh set	Grid points (×10^6)	H (m)	η (%)
Mesh1	0.24	7.62	89.91
Mesh2	1.11	7.71	89.97
Mesh3	2.48	7.88	90.43
Mesh4	3.45	7.92	90.55
Mesh5	5.98	8.02	90.61
Mesh6	6.73	7.99	90.63

3.3. Numerical methods

Within the axial flow pump, the flow is treated as incompressible. The equations of continuity, and momentum are listed in Cartesian coordinates as follows [10]:

$$\frac{\partial u_i}{\partial x_i} = 0 \tag{1}$$

$$\frac{\partial(\rho u_i)}{\partial t} + \frac{\partial(\rho u_i u_j)}{\partial x_i} = -\frac{\partial p}{\partial x_i} + \frac{\partial}{\partial x_j}\left[\mu\left(\frac{\partial u_i}{\partial x_j} + \frac{\partial u_j}{\partial x_i}\right)\right] \tag{2}$$

where u_i (i, j=1,2,3) represents the velocity component, and x_i (i, j=1,2,3) stands for the coordinate component. p stands for the static pressure, ρ is the fluid density, and μ is the dynamic viscosity.

The Reynolds-averaged Navier-Stokes equations are solved using the ANSYS-CFX commercial CFD code. At the same time, the k-ω SST turbulence model is selected. Regarding boundary conditions, the total pressure is specified at the inlet plane, while the outlet plane of the pump is defined by the mass flow rate. Furthermore, the solid surfaces of the flow passage are designated as no-slip and characterized by a smooth wall condition.

The impeller's flow passage is established within the rotational coordinate system, while other components such as the volute casing, inlet pipe, and outlet pipe are situated within the stationary coordinate system. The interface linking the rotational and stationary coordinate systems employs the sliding technique. For advection, the high-resolution scheme is employed, while the other transient terms are managed using the second-order backward Euler scheme. In the realm of steady simulation, the root-mean-square (RMS) residual is maintained below 10^{-6}.

It is noted that the present numerical simulation methods are suitable for predicting hydraulic performance as well as the internal flows in axial flow pumps based on our previous research [40, 41]. In this paper, given that the primary objective is to optimize the pump impeller, the assessment involves the comparison of hydraulic performance between the initial pump and the optimized pump.

3.4. Optimization algorithm

The optimization of axial flow pump impeller employs a machine learning-based algorithm with a dynamic sampling method. This methodology, inspired by Owoyele [36], involves utilizing machine learning models to guide the selection of computational points toward the most promising regions. The flowchart illustrating the machine learning-based algorithm can be seen in Figure 5.

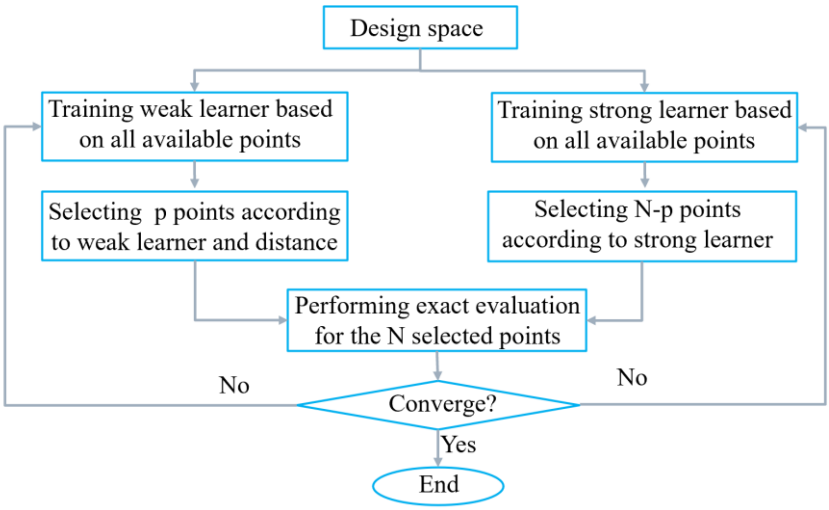

Figure 5. Flowchart of the machine-learning based algorithm.

Different from other optimization approaches, the current machine learning-based algorithm employs a deterministic strategy at each sampling step. The core methodology of this algorithm centers on utilizing two distinct categories of machine learning algorithms to facilitate dynamic exploration and exploitation within the design space. The initial category, referred to as the "weak learner," offers general insights into the response surface, thereby contributing to the exploration of the design space. During the exploration phase, evaluations derived from both the weak learner and the distance criteria are merged. This amalgamation generates sample points that effectively span the entire design space, while concurrently evading potential entrapment within local optima. Traditionally, the distance criterion is defined as the smallest Euclidean distance i.e. SED between two points, as exemplified in Equation 3.

$$\mathrm{SED}(A) = \min_{a_i \in A} \sqrt{\sum_{k=1}^{d} \left| a_i^k - a^k \right|^2} \tag{3}$$

where, d represents the dimension of the design space, a is a sample within the hypercube $[-1,1]^d$, A denotes the experimental design that involves the incremental selection of sample points, with the total number of samples unknown at any given time during the construction phase.

As shown Equation 3, the significance of SED(A) lies in representing the smallest Euclidean distance between a given point and all other existing sample points within the space. To ensure the space-filling nature of sample points selected by the distance criterion, the algorithm is designed to choose points that maximize SED(A) value. However, when dealing with optimization involving a high-dimensional design space, it's essential to also consider properties like projectiveness and non-collapsibility to enhance sample efficiency. This implies that for each point a^i, uniqueness in each dimension is sought, rendering it distinct from other points in every dimension. This projective property can be defined as the minimum projected distance i.e. MPD of points from each other, as defined in Equation 4.

$$\mathrm{MPD}(A) = \min_{a_i \in A} \min_{1 \le k \le d} \left| a_i^k - a^k \right| = \min_{a_i \in S} \left\| a_i - a \right\|_{-\infty} \tag{4}$$

The physical meaning of the Equation 4 representing the minimum projection distance along any individual dimension of a given point with respect to any other existing points within the design space. This understanding implies that by favoring points that maximize MPD value, the selection of two points projected onto the same location when mapping the d-dimensional space into a (d-1)-dimensional space along any axis can be averted. In light of the aforementioned discussion, and with the aim of selecting sample points that maximize both SED and MPD, an integrated distance evaluation criterion SEMPD is proposed in this study to nominate sample points during the exploration period, as formulated in Equation 5.

$$\mathrm{SEMPD}(A, a) = \frac{(n+1)^{1/d-1}}{2} \min_{a_i \in A} \sqrt{\sum_{k=1}^{d} \left| a_i^k - a^k \right|^2} + \frac{(n+1)}{2} \min_{a_i \in A} \min_{1 \le k \le d} \left| a_i^k - a^k \right| \tag{5}$$

where, n is number of existing sample points.

Incorporating this comprehensive distance evaluation criterion, the nominees are further refined by the weak learner. For every pre-sampled candidate point, the SEMPD criterion is calculated, and the optimal candidate is singled out to join the fold during the exploration phase. This approach ensures that the samples chosen through the exploration process not only embrace global insights but also uphold the space-filling nature. By selecting the nominee positioned farthest from the already sampled points, this methodology aids in the thorough exploration of the design space, which will contribute to sufficiently explore the design space and avoid being trapped into local optimum.

The second algorithm type furnishes more comprehensive insights into the promising region pinpointed by the weak learner, and is aptly termed the "strong learner". The primary role of the strong learner is to pinpoint sample points that are in close proximity to the best-estimated optimum within the design space. Through coordinated efforts, the weak and strong learners synergize to render decisions that are more effective during the optimization process. This harmonious interplay enables the algorithms to intelligently allocate denser sampling around the promising region while employing sparser sampling in less favorable areas. In this algorithmic framework, support vector regression is chosen as the foundational function model for the weak learner, while a committee machine consisting of multiple artificial neural networks collaborates as the strong learner. To penalize off-edge data points, we set the cost parameter of the weak learner Support Vector Regression to 18. The kernel parameter is the inverse of the feature count. Moreover, the parameter governing the number of support vectors is set to 0.6. The multiple neural networks used as the strong learner in this study had two layers with ten neurons each. With a constant learning rate of 0.08, we used the Adam optimizer to adjust the artificial neural network's weights.

As illustrated in Figure 5, as mentioned earlier, the process involves two distinct phases for each design iteration: an exploration phase (utilizing the weak learner) and an exploitation phase (leveraging the strong learner). To strike a well-tempered equilibrium between thorough exploration and efficient exploitation of the entire design space, this study introduces a dynamic mechanism for selecting design points. By adjusting the ratio of design points garnered from the exploration phase i.e. p to those from the exploitation phase i.e. N-p, a dynamic sampling approach is achieved. This approach strategically allocates a greater reliance on the weak learner during the early stages of the

optimization process, while gradually shifting the emphasis towards the strong learner as the global optimum is approached. This dynamic balance between exploration and exploitation optimizes the deterministic sampling of design points across the entire design space during each iteration step.

The flowchart of the optimization of axial flow pump combined with the machine learning based algorithm is shown in Figure 6. A fully automatic platform especially designed for the axial flow pump is established. After the parameterization of the axial pump impeller and defining the design space, with the machine learning based algorithm with dynamic sampling method, a series of sample points can be produced during one iteration. For each newly selected point, the design parameter values can be further derived. To evaluate the fitness function of the newly selected points for each iteration, a fully automatic evaluation process is set up, consisting of new impeller geometry generating, structural mesh generating, CFD simulation and fitness function evaluation. Then the result of the fitness function evaluation is further fed back to the optimizer for the next step of optimization iteration. This process continues to loop until the iteration converges.

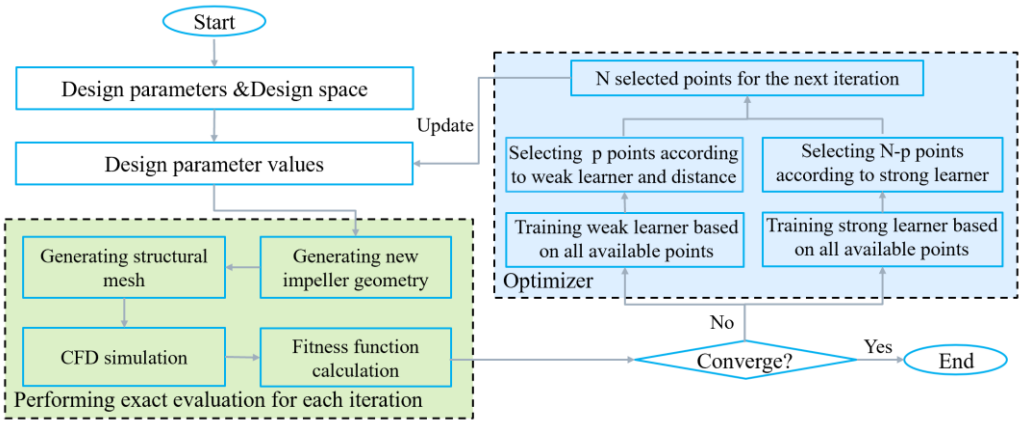

Figure 6. Optimization for axial impeller using machine learning based algorithm.

In the optimization of the axial flow pump impeller, the primary goal is to maximize the pump's efficiency under the design condition, while also ensuring that the pump head remains within the range of the designed value i.e. H_d and does not exceed $1.2H_d$. Thus, a fitness function is formulated by combining the efficiency and pump head, as demonstrated in Equation 6.

$$z = \eta - f(H) \tag{6}$$

where $f(H)$ represents the penalty function.

The penalty function $f(H)$ incorporates the designed pump head i.e. H_d as the main constraint. The penalty is activated when the head of the axial flow pump falls below H_d or exceeds $1.20H_d$. Consequently, the penalty function $f(H)$ is defined as follows:

$$f(H)=\begin{cases} \left(1-\dfrac{H}{H^0}\right)\times 100, H \le H^0 \\ 0,\ H^0 \le H \le 1.2H^0 \\ \left(\dfrac{H}{H^0}-1\right)\times 100, H \ge 1.2H^0 \end{cases} \tag{7}$$

where H^0 is the pump head under the optimization condition, i.e. the designed pump head H_d.

Figure 5 provides an overview of the comprehensive automatic optimization loop. At the beginning of the optimization, a set of initial design points are selected randomly to trigger the whole optimization process. Then perform the exact evaluation of the fitness function by means of generating new impeller geometry, generating structural mesh and the CFD simulation. Output the results to the

optimizer and obtain new design points for the next iteration. This iterative process is iterated until the solver either converges or attains the maximum threshold of design iterations.

4. Results and discussions

4.1. Performance improvement and geometry optimization

Figure 7 shows a clear comparison of the pump head between the initial and optimized pumps, while Figure 8 illustrates the efficiency comparison. Notably, the hydraulic performance, including pump head and efficiency, is determined through numerical simulation outcomes for both axial flow pumps. In comparison to the initial pump, the optimized version demonstrates a noticeable increase in pump head and enhanced efficiency within the flow rate range of $0.8Q_d$ to$1.2Q_d$. Substantial improvements are evident in Table 4, where the optimized pump achieves an efficiency of 92.62%, showcasing a significant 2% enhancement compared to the initial pump, specifically at the designated flow rate of Q_d. Particularly, for flow rates below Q_d, the efficiency of the optimized pump exhibits a robust increase of over 2%, surpassing the initial pump's performance. Thus, the impeller optimization is successful for the axial flow pump.

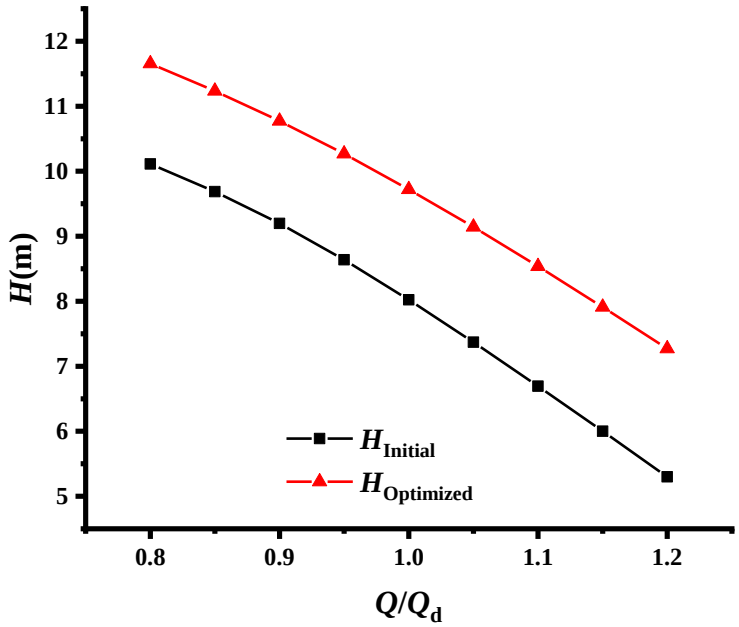

Figure 7. Pump head for axial flow pumps.

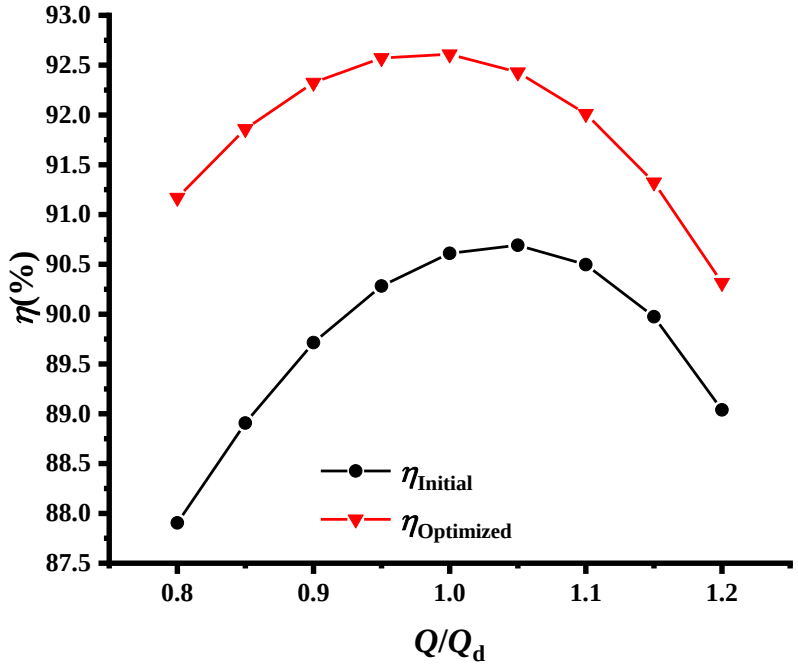

Figure 8. Hydraulic efficiency for axial flow pumps.

Table 4. Hydraulic performance of initial and optimized pumps under design flow rate.

Axial flow pump	H(m)	η(%)
Initial	8.02	90.61
Optimized	9.72	92.62

The impellers for the initial and the optimized axial flow pumps are illustrated in Figure 9, where Figure 9(a) is the upstream view of the impeller, and Figure 9(b) is the downstream view of the impeller, Figure 9(c) is the side view and Figure 9(d) is the front view of the impeller. As can be observed from the geometry comparison shown in Figure 9, the optimized impeller has an obvious change in the rake and skew angle. Generally, the blade section profile at impeller hub is short, and that at impeller shroud is long for the initial pump based on the conventional design. However, for the optimized impeller, the blade section profile has the roughly equivalent length both at impeller hub and shroud. It is also seen that there is a rake of 10.2° as shown in Figure 9(c) and skew of 23.5° as shown in Figure 9(d) at blade leading edge of the optimized impeller. Besides, other blade geometrical parameters of the initial and optimized impellers are shown in Table 5. These changes are helpful to guide the design optimization for the axial flow pumps in the future.

Table 5. Blade geometries for the initial and optimized impellers.

Parameters	Symbol	Value for initial impeller	Value for optimized impeller
Circumferential angle at leading edge of mean camber line at shroud	$\varphi_{le,s}$	11.4	16.8
Circumferential angle at trailing edge of mean camber line at hub	$\varphi_{te,h}$	70	94.6
Circumferential angle at trailing edge of mean camber line at shroud	$\varphi_{te,s}$	70	71.1
Incidence angle at hub	Δi_{hub}	0°	-6.3°
Incidence angle at shroud	Δi_{shroud}	0°	-4.3°
Slip angle at hub	$\Delta\delta_{hub}$	19.8°	15.8°
Slip angle at shroud	$\Delta\delta_{shroud}$	3.5°	17.4°

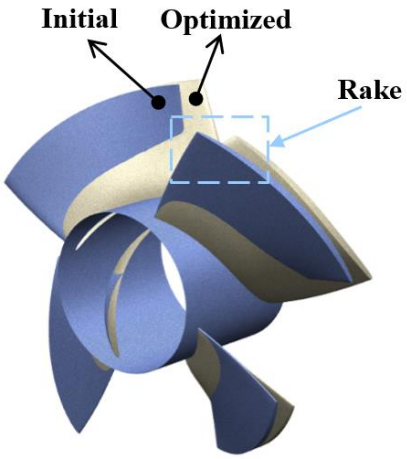

(a) Upstream side isometric view

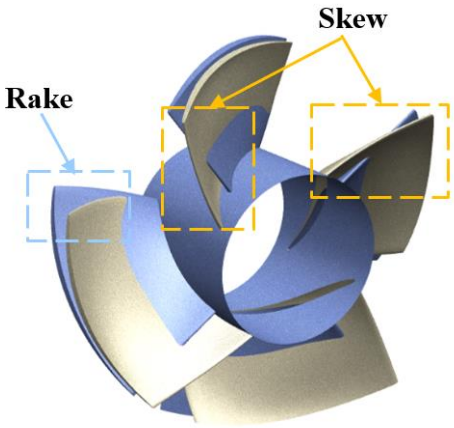

(b) Downstream side isometric view

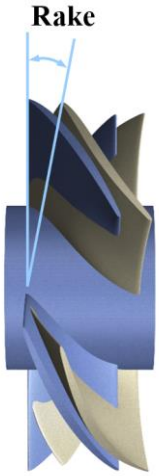

(c) Side view

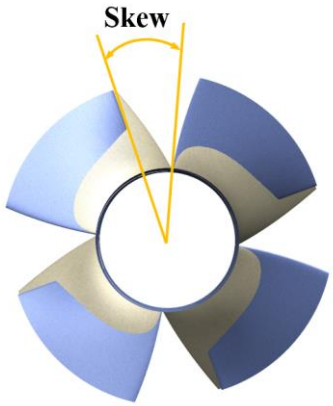

(d) Front view

Figure 9. Blade geometry for the initial and optimized impellers.

4.2. Entropy generation rate comparison

In order to investigate the effect of impeller optimization on performance improvement for the axial flow pump, the energy loss should be considered.

The viscous flow as well as the turbulence dissipation inevitably leads to the energy loss in the axial flow pump, which is highly correlated with the pump efficiency. As an adiabatic device, the energy loss directly relates to the generation of entropy. In this study, the entropy generation is used to analyze the total energy loss quantitatively. The total entropy production rate (EPR) can be calculated by the Equation 8.

$$\dot{S}_{\text{total}} = \dot{S}_{\bar{\text{D}}} + \dot{S}_{\text{D}'} + \dot{S}''_{\text{W}} \tag{8}$$

where $\dot{S}_{\text{total}}$ represents the total entropy generation rate, comprising three distinct components: $\dot{S}_{\bar{\text{D}}}$, denoting the entropy generation attributed to the time-averaged velocity (EPDD); $\dot{S}_{\text{D}'}$, reflecting the entropy production rate arising from fluctuating velocity (EPTD); and $\dot{S}''_{\text{W}}$, capturing entropy generation within the vicinity of the wall region (EPWS).

The precise descriptions of these three terms are elucidated in equation (6). Notably, within the context of the Reynolds-averaged Navier-Stokes (RANS) model, specifically the *k-ω* turbulence model, the entropy production rate stemming from the fluctuating velocity component can be computed using the expression outlined in Equation 9:

$$\dot{S}_{\bar{\text{D}}} = \frac{\mu_{\text{eff}}}{T}\left[2\left\{\left(\frac{\partial U}{\partial x}\right)^2 + \left(\frac{\partial V}{\partial y}\right)^2 + \left(\frac{\partial W}{\partial z}\right)^2\right\} + \left(\frac{\partial U}{\partial y} + \frac{\partial V}{\partial x}\right)^2 + \left(\frac{\partial U}{\partial z} + \frac{\partial W}{\partial x}\right)^2 + \left(\frac{\partial V}{\partial z} + \frac{\partial W}{\partial y}\right)^2\right]$$

$$\dot{S}_{\text{D}'} = \beta \frac{\rho \omega k}{T}$$
$$\dot{S}''_{\text{W}} = \frac{\vec{\tau} \cdot \vec{v}_{\text{W}}}{T} \tag{9}$$

where *U*, *V*, *W* is the time averaged velocity in *x*, *y*, *z* direction respectively based on Reynolds time averaged. *k* is turbulent kinetic energy, and *ω* is turbulent eddy frequency. *T* is the absolute temperature. β is the coefficient, =0.09 [42]. $\vec{\tau}$ is the wall shear stress, and $\vec{v}_{\text{W}}$ is the first grid cell velocity near the wall. μ_{eff} is the effective viscosity, and can be calculated as

$$\mu_{\text{eff}} = \mu + \mu_{\text{tur}} \tag{10}$$

where μ_{tur} is the turbulent viscosity.

For the impeller blade, as a wall region, the total entropy generation mainly originates from the EPWS term. Figure 10 shows the contours of EPWS on the blade pressure side of the impeller for the initial pump and optimized pump. It can be seen that there is a high value region of EPWS, locating near the shroud from the leading edge of blade pressure side for the initial impeller. On the other hand, the area of this region much decreases, and the region with very low EPWS at the trailing edge increases for the optimized impeller. The distribution of EPWS indicates relatively smaller flow loss around the blade side for the optimized impeller, and is helpful for the improvement of the hydraulic efficiency for the optimized pump.

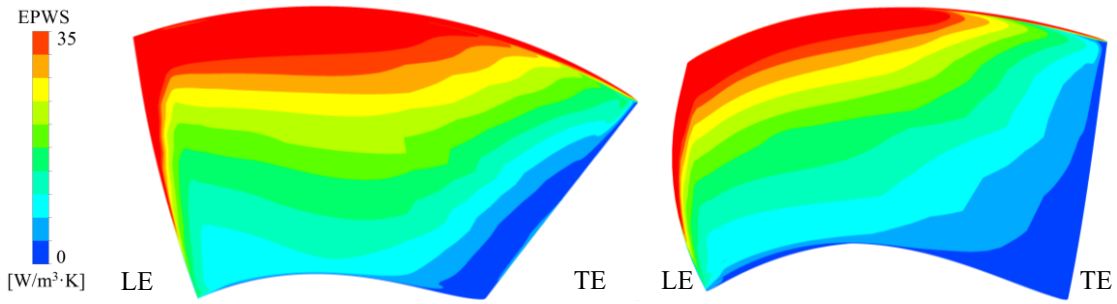

(a) Initial impeller (b) Optimized impeller

Figure 10. EPWS distribution on blade pressure side for two impellers.

Figure 11 presents the EPR distribution at three different span-wise sections near the impeller hub for two pumps. Span0.1, Span0.2 and Span0.3 mean the span-wise sections of 10%, 20% and 30% blade width. As illustrated in the figure, a high value region can be observed at the trailing edge, indicating that there is a relatively large energy loss at the outlet region for both impellers. Compared with the initial impeller, the optimized impeller has a smaller area for the high value region of entropy generation rate near the impeller exit. At the section of Span0.1, there is an extra area for the high value region of entropy generation rate in the initial impeller. Thus, the energy loss in the initial impeller will be larger than that in the optimized impeller.

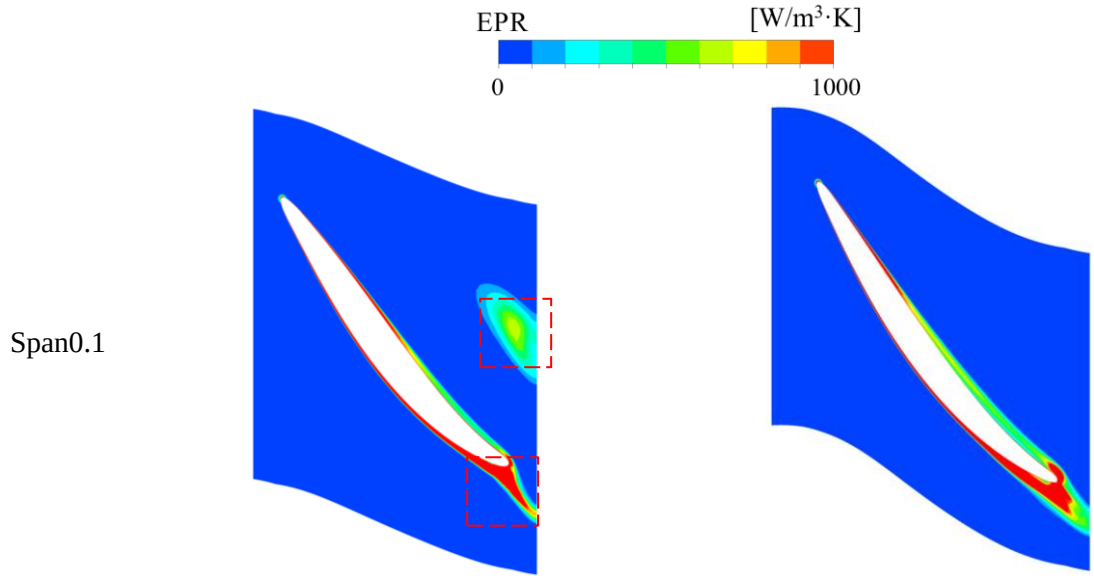

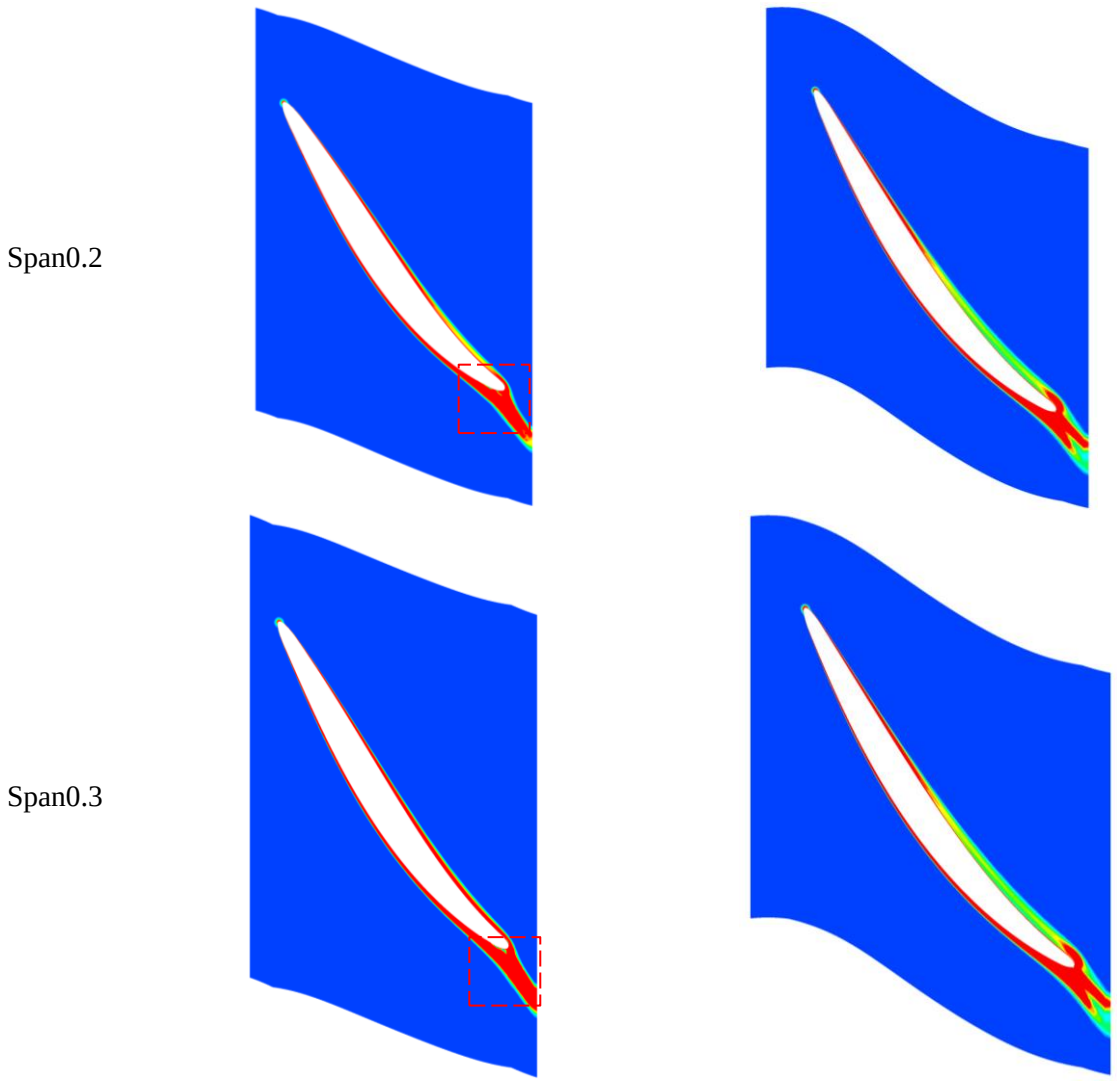

Figure 11. EPR distribution at different span-wise sections near the hub.

It is noted that there is a tip clearance between the impeller blade shroud and pump casing for the axial flow pumps. Due to the high pressure difference between the pressure side and the suction side of the impeller blade, the strong tip clearance flow usually induces great energy loss. In Figure 12, the EPR distribution at several stream-wise sections near tip clearance is shown for the initial and optimized pumps. For better understanding, the iso-surface of swirling strength at 322[s^{-1}] is also plotted in the same figure. It is clear that there exists a region with high EPR value at the tip clearance, and a strong vortex occurs near the blade suction side in blade-to-blade flow passage. The vortex is correlated with the mixing of the tip clearance flow and the main flow, and induces the increase of energy loss in the axial flow pump. It is also seen that the vortex in the initial impeller moves toward the main flow channel, while the vortex moves along the blade suction side in the optimized impeller. Therefore, the interaction between the vortex and the main flow in the optimized impeller is weaker than that in the initial impeller, and this makes less energy loss in the optimized impeller.

Totally, the area of high EPR value is alleviated for the optimized impeller, and this optimization is helpful for hydraulic performance improvement for the axial flow pump.

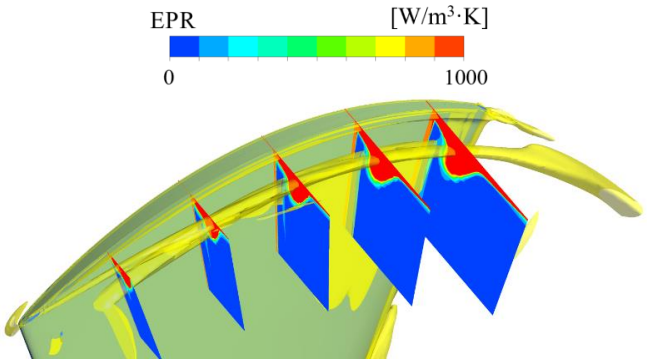

(a) Initial impeller

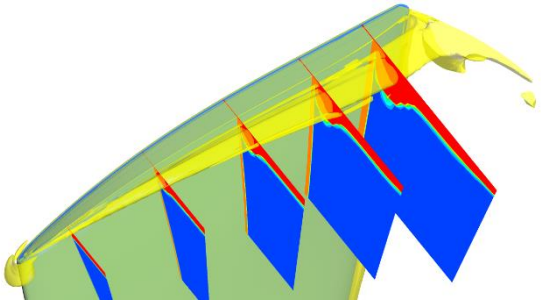

(b) Optimized impeller

Figure 12. EPR distribution near blade tip clearance with iso-surface of swirling strength at 322 s^{-1}.

4.3. Internal flow

To have a better understanding of the reason why hydraulic performance of the optimized pump has been improved, the internal flow analysis has been carried out based on simulation results.

The distribution of pressure coefficient along impeller blade for the axial flow pumps is depicted in Figure 13. Note that the pressure coefficient C_p is defined by Equation 11.

$$C_p = \frac{2(p - p_\infty)}{\rho v_\infty^2} \tag{11}$$

where p represents the static pressure. p_∞ stands for the reference pressure at impeller inlet. ρ is the density of the fluid and v_∞ represents the velocity at impeller inlet.

As shown in Figure 13, at all span-wise sections the minimum pressure coefficient at the blade leading edge for the optimized impeller is much higher than that for the initial impeller. If the pressure difference between blade pressure side and suction side at the same stream-wise location can be regarded as the blade load, it is very clear that the optimization changes the blade load for the axial flow pump. Especially, the blade load is large at the leading edge for the initial impeller, but that much decreases for the optimized impeller. The pressure distribution of the optimized pump is beneficial to improve cavitation performance. Generally, the blade load for the optimized impeller becomes uniform compared with the initial impeller. From the span-wise section of 50% blade width to that of 90% blade width, the blade loads are larger for the optimized impeller, indicating the higher pump head compared with the initial impeller.

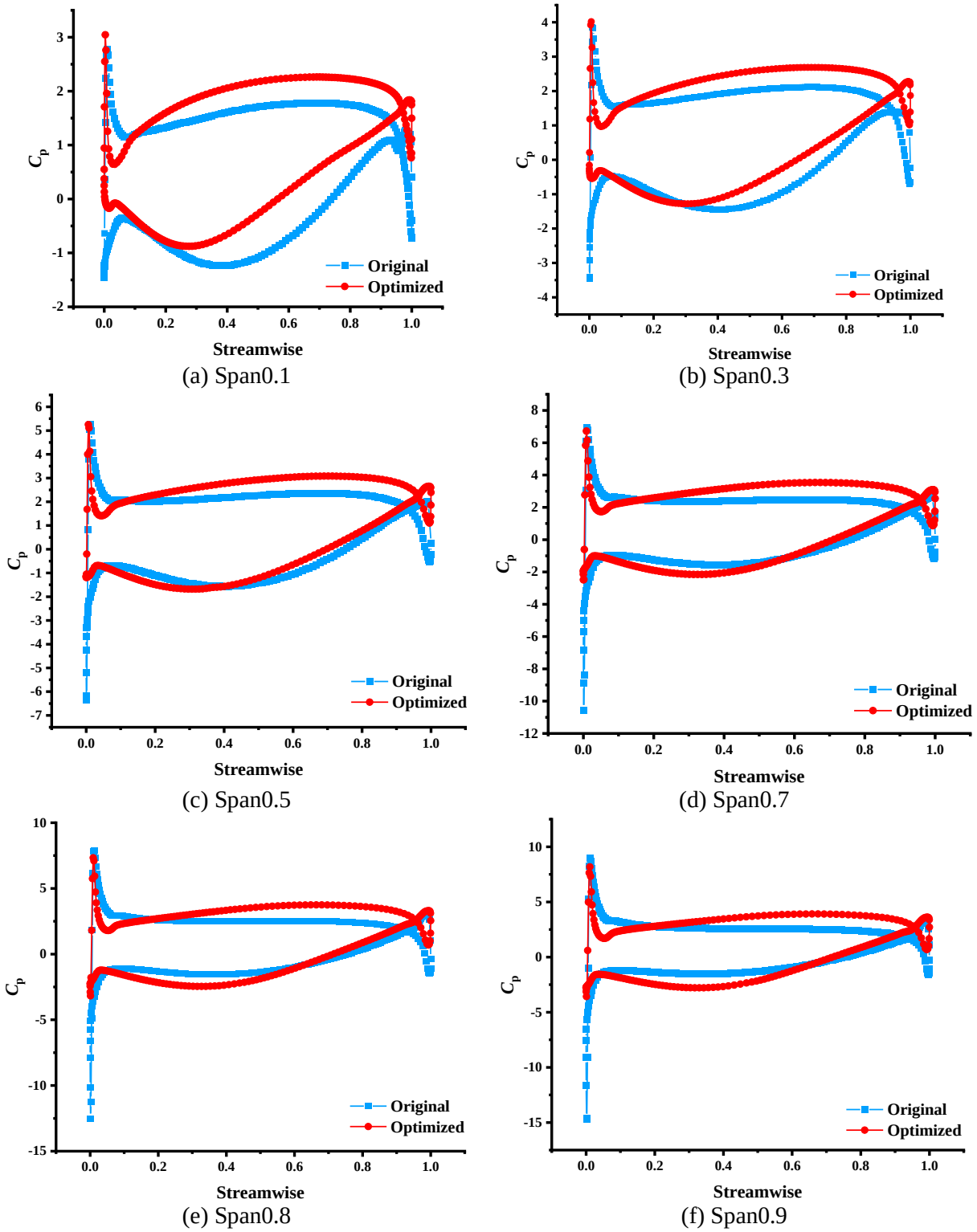

Figure 13. Pressure distribution at different span-wise sections.

The streamline distribution at pressure side is visualized in Figure 14 for the initial and optimized impellers. For two impellers, the streamlines at blade leading edge is smooth, and tends to move upward at trailing edge from the hub. It is clear that the streamline distribution of the optimized

impeller is much more uniform compared with the initial impeller.

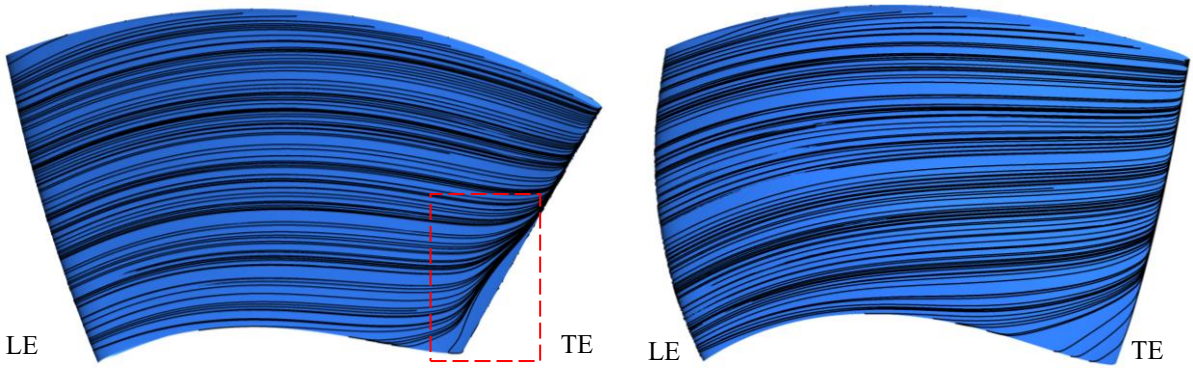

(a) Initial impeller (b) Optimized impeller

Figure 14. Streamline distribution at blade pressure side.

Further, the velocity distribution near blade pressure side is shown in Figure 15 for the initial and optimized impellers. It is noted that there are the high velocity zone at leading edge and blade tip, and the low velocity zone at the trailing edge near the hub for the initial impeller. However, the velocity distribution near the blade pressure side becomes much more uniform for the optimized impeller.

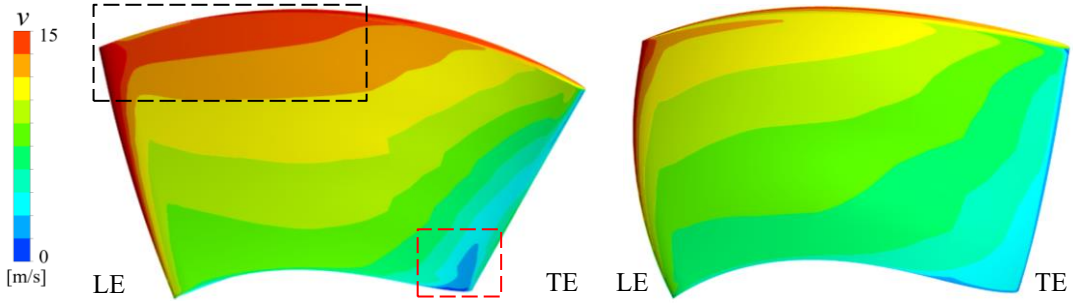

(a) Initial impeller (b) Optimized impeller

Figure 15. Velocity distribution near blade pressure side.

In the blade-to-blade flow passage of the impeller, the radial velocity due to the rotating effect promotes the secondary flow. It is seen that the radial velocity near the blade pressure side is shown in Figure 16. Basically the radial velocity increases from leading edge to trailing edge, indicating the development of the secondary flow in the impeller. The averaged radial velocity for the initial impeller is larger compared with the optimized impeller. Particularly, there are two zones with large radial velocity, i.e. the trailing edge near the hub and the leading edge near the blade tip in the initial impeller. Through optimization, the zone with large radial velocity at leading edge near blade tip disappears, and that at trailing edge near the hub is much restricted for the optimized impeller.

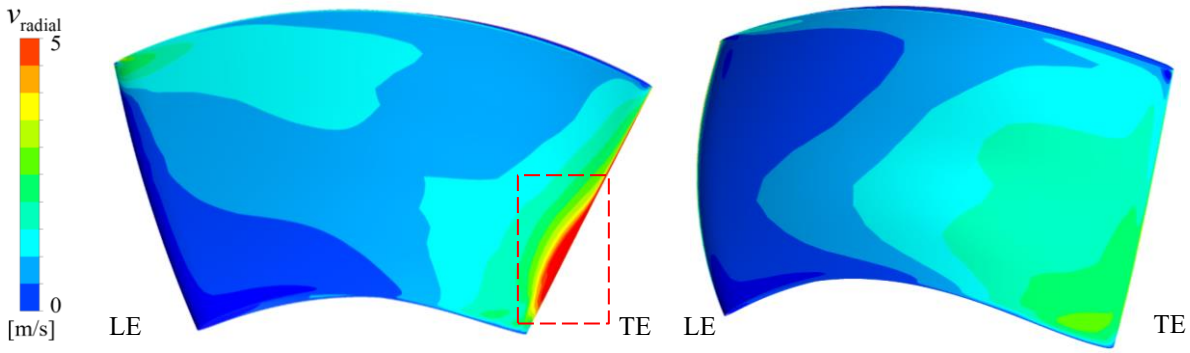

(a) Initial impeller (b) Optimized impeller

Figure 16. Radial velocity distribution near blade pressure side.

Figure 17 shows the streamline distribution at three span-wise sections near the hub. As illustrated in the figure, there exists a flow separation at the trailing edge, which will cause the sudden rise of hydraulic loss at the outlet region for the initial impeller. On the contrary, the flow separation is greatly alleviated for the optimized impeller.

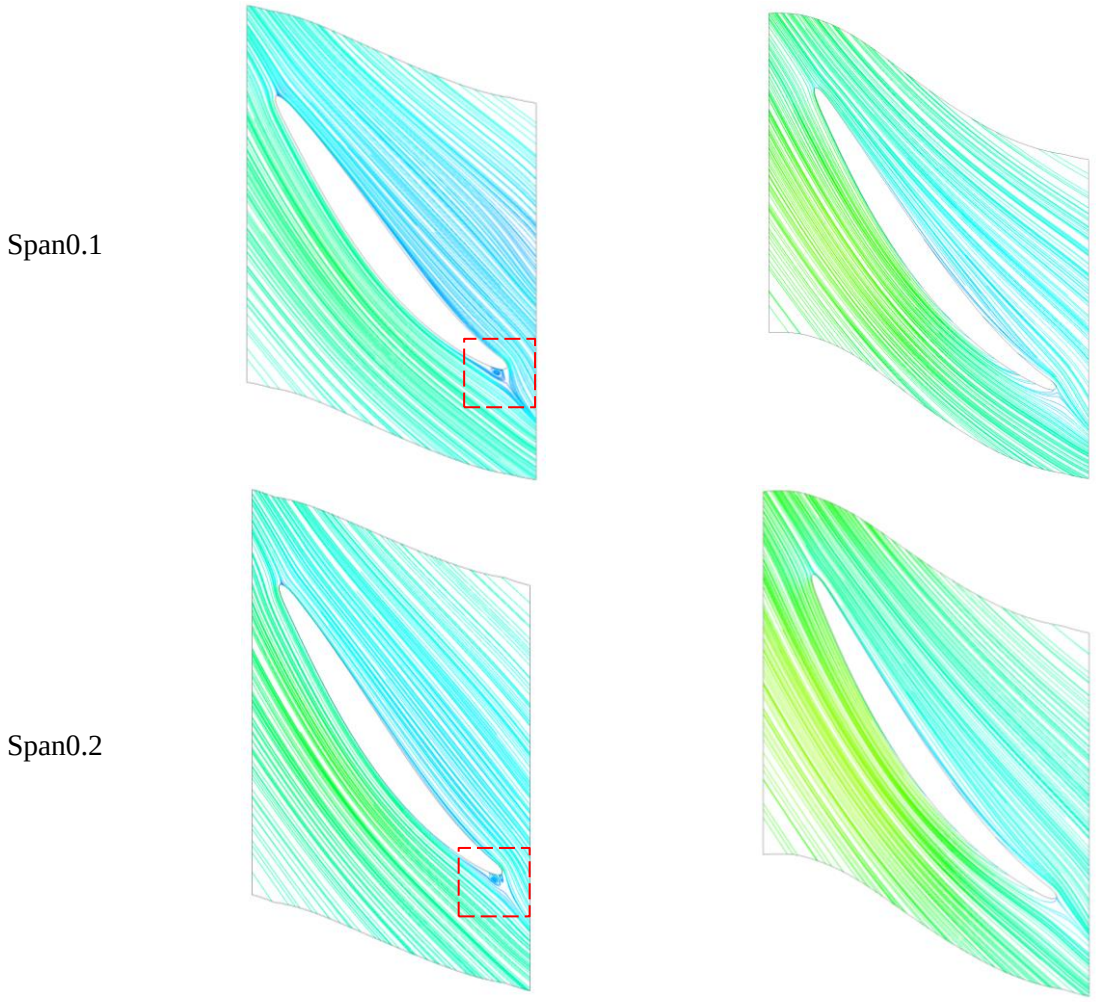

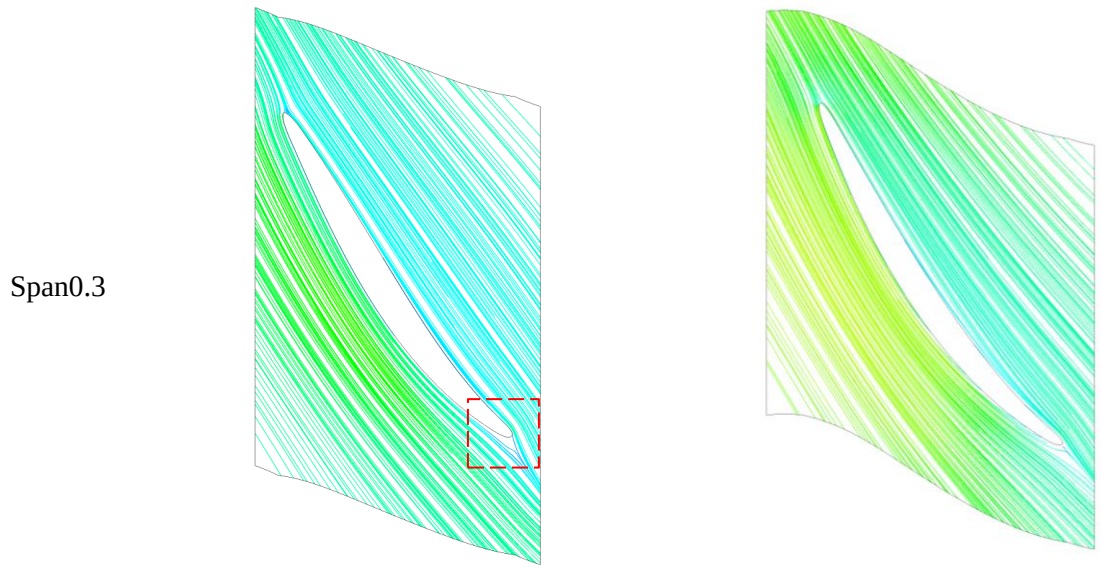

(a) Initial impeller (b) Optimized impeller

Figure 17. Streamline distribution at different span-wise section near the hub.

As the useful tool for flow diagnosis, the boundary vorticity flux i.e. BVF is introduced to investigate the flow characteristics in the axial flow pump. As indicated in the references [43, 44], the application of BVF combined with the lines of wall friction can serve as the criterion of the flow separation for an arbitrary three-dimensional curved surface. The flow separation usually occurs around the place where the peak value region of BVF and the convergence of the wall friction lines can be observed simultaneously. The definition of BVF is shown in Equation 12.

$$\mathrm{BVF} = \sigma = \sigma_{\mathrm{a}} + \sigma_{\mathrm{p}} + \sigma_{\mathrm{vis}}$$
$$\sigma_{\mathrm{a}} = \vec{n} \times \vec{a}; \sigma_{\mathrm{p}} = \frac{1}{\rho} \vec{n} \times \nabla p; \sigma_{\mathrm{vis}} = \nu \left(\vec{n} \times \nabla \right) \times \Omega \tag{12}$$

where $\vec{n}$ is the unit normal vector that pointing out from the fluid.

Figure 18 presents the BVF and wall friction lines distribution on blade pressure side under the design flow rate condition.

As shown in Figure 18(a), there is the peak value region of BVF located at the trailing edge for the initial impeller. Meanwhile, the convergence of the wall friction lines can be observed at the trailing edge near the hub. These results indicate that the vortex at the trailing edge has negative effect on the torque for the initial impeller. Based on the results shown in Figure 14(a) and Figure 17(a), it can be further confirmed that there will be the occurrence of the flow separation near blade trailing edge where a peak value region of BVF and the convergence of the wall friction lines happen.

As for the optimized impeller, it can be seen that the BVF distributed on blade pressure side is more uniform, and the region with peak BVF value near blade tip from the leading edge is greatly alleviated compared with the initial impeller. Although there still exists a relatively small region of high BVF value at the trailing edge near the hub, the wall friction line is fairly smooth, and no convergence occurs. Therefore, the flow at the impeller exit is more uniform with no obvious separation, ant that is consistent with the results shown in Figure 14(b) and Figure 17(b). Furthermore, based on the flow diagnosis utilizing BVF and the wall friction lines, it is clear that the vortex at blade trailing edge is eliminated after the optimization, and the improvement of internal flow results in better hydraulic performance for the axial flow pump.

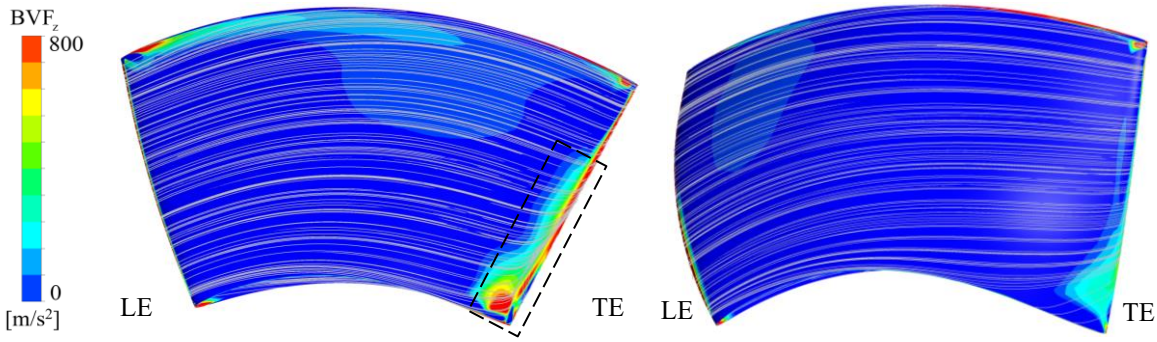

(a) Initial impeller (b) Optimized impeller

Figure 18. Boundary vorticity flux and wall friction line distribution at blade pressure side.

5. Conclusions

A machine learning-based algorithm with dynamic sampling method has been proposed for the optimization of axial pump impeller. Hydraulic performance and internal flow characteristics of the pumps are assessed through CFD analysis, and compared between the initial and optimized impellers. From the obtained results, the following conclusions can be drawn:

(1) The machine learning-based approach has effectively optimized the axial flow pump impeller. The optimized impeller has better hydraulic performance compared with the initial design.

(2) The impeller optimization has remarkably improved the internal flow of the axial pump. The pump with optimized impeller has more uniform flow pattern near the blade pressure side, while effectively mitigating flow separation at the blade trailing edge near the hub compared with that with the initial impeller.

(3) The pump with optimized impeller achieves higher pressure at the blade's leading edge compared with the pump with the initial impeller. This favorable pressure distribution along the blade may improve cavitation performance for the axial flow pump.

Acknowledgments

This research was supported by the National Natural Science Foundation of China (Project No. 52006232), the Open Research Fund of Key Laboratory of Space Utilization, Chinese Academy of Sciences (No. LSU-KFJJ-2021-04), and the Tsinghua National Laboratory for Information Science and Technology.

References

[1] Qiu J T, Yang C J, Dong X Q, Wang Z L, Li W and Noblesse F 2018 Numerical simulation and uncertainty analysis of an axial-flow waterjet pump *J. Mar. Sci. Eng.* **6(2)** pp 71.

[2] Zhao X, Chen T, Huang B and Wang G 2022 Numerical analysis of the cavitating flow in an axial flow waterjet pump with special emphasis on the tip leakage flow and tip leakage vortex *J. Phys. Conf. Ser.* **2217(1)** 012018.

[3] Zhao X, Liu T, Huang, B and Wang G 2020 Combined experimental and numerical analysis of cavitating flow characteristics in an axial flow waterjet pump *Ocean Engineering* **209**(June) 107450.

[4] Zhang D, Shi W, van Esch B P M, Shi L and Dubuisson M 2015 Numerical and experimental investigation of tip leakage vortex trajectory and dynamics in an axial flow pump *Computers and Fluids* **112** pp 61–71.

[5] Zhang W, Hu Q and Zhou Y 2020 Effects of an inlet vortex on the performance of an axial-flow pump *Energies* **13(11)** pp 2854.

[6] Song X Y, Li H Y, Li Yand Luo X 2022 The development of a high-speed miniature pump with dynamic bearing *J. Phys. Conf. Ser.* **2217(1)** 012049.

[7] Yang F, Li Z, Fu J, Lv Y, Ji Q and Jian H 2022 Numerical and Experimental Analysis of Transient Flow Field and Pressure Pulsations of an Axial-Flow Pump Considering the Pump-Pipeline Interaction *J. Mar. Sci. Eng.* **10(2)** pp 258.
[8] Xie R S, Tang F P, Yang F and Xiang C 2018 Effect of the flow in blade root-leakage on hydraulic characteristic in axial flow pump system *IOP Conf. Ser.: Earth Environ. Sci.* **163(1)** 012123.
[9] Zhu H, Bo G, Zhou Y, Zhang R and Cheng J 2018 Pump Selection and Performance Prediction for the Technical Innovation of an Axial-Flow Pump Station *Math. Probl. Eng.* **2018** 6543109.
[10] Yang F, Lin Z, Li J, Nasr A, Cong W and Li C 2022 Analysis of internal flow characteristics and structure optimization of vertical submersible axial flow pump device *Adv. Mech. Eng.* **14(5)**.
[11] Song X, Yu W, Pan X and Luo X 2021 Energy balance analysis for a canned motor pump used for heat supply system *J. Phys. Conf. Ser.* **1909(1)** 012072.
[12] Xiang H, Chen J, Cheng J and Song X 2022 Blade Number Selection for a Splittered Mixed-Flow Compressor Impeller Using Improved Loss Model *Int. J. Turbo Jet Engines* **39(4)** pp 549-564.
[13] Kergourlay G, Younsi M, Bakir F and Rey R 2007 Influence of splitter blades on the flow field of a centrifugal pump: Test-analysis comparison *Int. j. rotating mach*.
[14] Yuan Y and Yuan S 2017 Analyzing the effects of splitter blade on the performance characteristics for a high-speed centrifugal pump *Adv. Mech. Eng.* **9(12)** pp 1-11.
[15] Ekradi K and Madadi A 2020 Performance improvement of a transonic centrifugal compressor impeller with splitter blade by three-dimensional optimization *Energy* **201** 117582.
[16] Montazeri M J and Ebrahimi R 2010 Multidisciplinary optimization of a pump-fed system in a cryogenic LPE using a systematic approach based on genetic algorithm *Aerosp Sci Technol.* **49** pp 185-196.
[17] Zhang J, Cai S, Li Y, Zhou X and Zhang Y 2017 Optimization design of multiphase pump impeller based on combined genetic algorithm and boundary vortex flux diagnosis *J. Hydrodyn.* **29(6)** pp 1023-34.
[18] Lamba R, Kaushik S C and Tyagi S K 2018 Geometric optimization of trapezoidal thermoelectric heat pump considering contact resistances through genetic algorithm *Int. J. Energy Res.* **42(2)** pp 633-647
[19] Starke A R, Cardemil J M and Colle S 2018 Multi-objective optimization of a solar-assisted heat pump for swimming pool heating using genetic algorithm *Appl. Therm. Eng.* **142** pp 118-126.
[20] Ahmadi M H, Ahmadi M A, Bayat R, Ashouri M and Feidt M 2015 Thermo-economic optimization of Stirling heat pump by using non-dominated sorting genetic algorithm *Energy Convers. Manag.* **91** pp 315-322.
[21] Tao R, Xiao R, Yang W, Wang F and Liu W 2014 Optimization for cavitation inception performance of pump-turbine in pump mode based on genetic algorithm *Math. Probl. Eng.* **2014** 234615.
[22] Safikhani H, Khalkhali A and Farajpoor M 2011 Pareto based multi-objective optimization of centrifugal pumps using CFD neural networks and genetic algorithms *Eng. Appl. Comput. Fluid Mech.* **5(1)** pp 37-48.
[23] Xu K, Wang G, Zhang L, Wang L, Yun F, Sun W, Wang X and Chen X 2021 Multi-objective optimization of jet pump based on RBF neural network model *J. mar. sci.* **9(2)** pp 1-19.
[24] Huang R F, Luo X W and Ji B 2015 Multi-objective optimization of a mixed-flow pump impeller using modified NSGA-II algorithm *Sci. China Technol. Sci.* **58(12)** pp 2122-30
[25] Ghadimi B, Nejat A, Nourbakhsh S A and Naderi N 2019 Shape optimization of a centrifugal blood pump by coupling CFD with metamodel-assisted genetic algorithm *J. Artif. Organs.* **22(1)** pp 29-36.

[26] Shojaeefard M H, Hosseini S E and Zare J 2019 CFD simulation and Pareto-based multi-objective shape optimization of the centrifugal pump inducer applying GMDH neural network, modified NSGA-II, and TOPSIS *Struct. Multidiscip. Optim.* **60(4)** pp 1509-1525.
[27] Massoudi S, Picard C and Schiffmann J 2022 Robust design using multiobjective optimisation and artificial neural networks with application to a heat pump radial compressor *Design Science* **8(2009)** pp 1-32
[28] Pei J, Gan X, Wang W, Yuan S and Tang Y 2019 Multi-Objective Shape Optimization on the Inlet Pipe of a Vertical Inline Pump *J. Fluids Eng. Trans. ASME* **141(6)** 061108.
[29] Derakhshan S, Mohammadi B and Nourbakhsh A 2008 Incomplete sensitivities for 3D radial turbomachinery blade optimization *Computers and Fluids* **37(10)** pp 1354-63.
[30] Wang G G and Shan S 2007 Review of metamodeling techniques in support of engineering design optimization *J. Mech. Des. Trans. ASME* **129(4)** 370-380
[31] Gan X, Pei J, Wang W, Yuan S and Lin B 2022 Application of a modified MOPSO algorithm and multi-layer artificial neural network in centrifugal pump optimization *Engineering Optimization* **55(4)** pp 580-598.
[32] Ghadimi B, Nejat A, Nourbakhsh S A and Naderi N 2019 Multi-Objective Genetic Algorithm Assisted by an Artificial Neural Network Metamodel for Shape Optimization of a Centrifugal Blood Pump *Artif. Organs* **43(5)** pp E76-E93.
[33] Han X, Kang Y, Sheng J, Hu Y and Zhao W 2020 Centrifugal pump impeller and volute shape optimization via combined NUMECA, genetic algorithm, and back propagation neural network *Struct. Multidiscip. Optim.* **61(1)** pp 381-409.
[34] Zhao B, Wang Y, Chen H, Qiu J and Hou D 2015 Hydraulic optimization of a double-channel pump's impeller based on multi-objective genetic algorithm *Chin. J. Mech. Eng.* **28(3)** pp 634-640.
[35] Wang W, Osman M K, Pei J, Gan X and Yin T 2019 Artificial neural networks approach for a multi-objective cavitation optimization design in a double-suction centrifugal pump *Processes* **7(5)** pp 246.
[36] Owoyele O and Pal P 2021 A Novel Active Optimization Approach for Rapid and Efficient Design Space Exploration Using Ensemble Machine Learning *J. Energy Resour. Technol. Trans. ASME.* **143(3)** pp 1-8.
[37] Owoyele O and Pal P 2021 A novel machine learning-based optimization algorithm (ActivO) for accelerating simulation-driven engine design *Appl. Energy* **285**(January) 116455.
[38] Song X, Wang L and Luo X 2022 Airfoil optimization using a machine learning-based optimization algorithm *J. Phys. Conf. Ser.* **2217(1)** 012009.
[39] Yang J and Guan X 2008 Hydraulic design of high specific speed model axial-flow pump *Nongye Jixie Xuebao/Trans. Chin. Soc. Agric. Mach.* **39(12)** pp 89-92.
[40] Yang D, Zhao M, Ye W, Shen L and Luo X 2021 Numerical simulations of fish movement in axial pump using immersed boundary method *J. Hydroelectr. Eng.* **40(7)** pp 95-104.
[41] Yang D D, Zhao M X, Shen L and Luo X W 2022 Effects of operating condition on fish behavior and fish injury in an axial pump *Sci. China Technol. Sci.* **65(1)** 157-168.
[42] Yu A, Tang Y, Tang Q, Cai J, Zhao L and Ge X 2022 Energy analysis of Francis turbine for various mass flow rate conditions based on entropy production theory *Renewable Energy* **183** pp 447-458.
[43] Zhang Y X, Chen L, Zhou X, Jiang C W and Su M 2012 Hydraulic design, numerical simulation and BVF diagnosis of high efficiency centrifugal pump *IOP Conf. Ser.: Earth Environ. Sci.* **15**(PART 3).
[44] Zhou X, Zhang Y, Ji Z and Chen L 2014 The impeller improvement of the centrifugal pump based on BVF diagnostic method *Adv. Mech. Eng*.